ARMA 10-473

Comparison between elasto-plastic and rigid-plastic cohesive surface elements and embedded strong discontinuity finite element implementation of rock fracture

Regueiro, R.A. and Yu, S.-K.
Department of Civil, Environmental, and Architectural Engineering, University of Colorado at Boulder, Boulder, CO 80309, U.S.A.

This paper was prepared for presentation at the 44th US Rock Mechanics Symposium and 5th U.S.-Canada Rock Mechanics Symposium, held in Salt Lake City, UT June 27-30, 2010.

ABSTRACT: The paper presents a comparison between embedded strong discontinuity finite element implementation and elasto-plastic (EP) and rigid-plastic (RP) cohesive surface finite element (CSE) implementations of cracking/fracture in rock. It is shown that care must be taken when choosing the elastic stiffnesses for the EP CSE model, if they are to act as penalty parameters. The RP CSE and EDE implementations obviate this choice. Formulation and implementation is restricted to small strains and rotations, and numerical examples are conducted for two-dimensional (2D) plane strain.

1. INTRODUCTION

For clean rock fractures, or when the fracture aperture thickness is small relative to the boundary value problem spatial domain of interest, the interface between two rock faces (or between a grain and its cement matrix) can be approximated as a strong discontinuity (jump in displacement across a surface of zero measure, i.e., a crack); a weak discontinuity is a jump in strain across a shear or compaction band [6]. Computationally, using the finite element method, it is possible to model this strong discontinuity in various ways, some of which include the following: (1) discrete representation of the fracture surface using contact mechanics [1] or cohesive surface elements (CSE) [2]; or (2) embedded discontinuity approaches such as the extended finite element method (X-FEM) [3, 4] or the assumed enhanced strain (AES) method [5, 6, 7, 8, 9, 10]. This paper will focus on a comparison between a discrete approach (CSE) and an embedded discontinuity approach (AES). For the CSE, we will consider elasto-plastic and rigid-plastic formulations, where the rigid-plastic implementation is handled by an augmented-Lagrange multiplier approach [15, 16]. The elasto-plastic formulation typically chooses large values of cohesive surface elastic stiffnesses (normal and tangential directions) as penalty parameters. We will investigate this aspect as well. The embedded discontinuity approach defaults to a rigid-plastic cohesive surface model. Numerical examples will be presented in two dimensions.

The advantage of the CSE approach over the AES one is the ability to model microstructurally the micro-cracking in rock at grain/cement interfaces (two different materials: e.g., quartz silt grain embedded in clay matrix, Fig.1), whereas the current AES formulation is limited to simulating strong discontinuities in a single material.

Throughout the paper we assume small deformations and rotations. Symbolic notation is used for clearer presentation, such as the inner product of two second order tensors $(\boldsymbol{a}\cdot\boldsymbol{b})_{ik}=a_{ij}b_{jk}$, the contraction of two tensors $\boldsymbol{a}:\boldsymbol{b}=a_{ij}b_{ij}$, or the dyadic product $(\boldsymbol{a}\otimes\boldsymbol{b})_{ijkl}=a_{ij}b_{kl}$. Tensor operators are used such as the symmetric gradient $(\boldsymbol{\nabla}^s\boldsymbol{v})_{ij}=(v_{i,j}+v_{j,i})/2$, and divergence $(\boldsymbol{\nabla}\cdot\boldsymbol{a})_i=a_{ij,j}$, where $(\bullet)_{,j}=\partial(\bullet)/\partial x_j$ denotes a partial spatial derivative. The symbol $(\dot{\bullet})=\partial(\bullet)/\partial t$ denotes a time derivative.

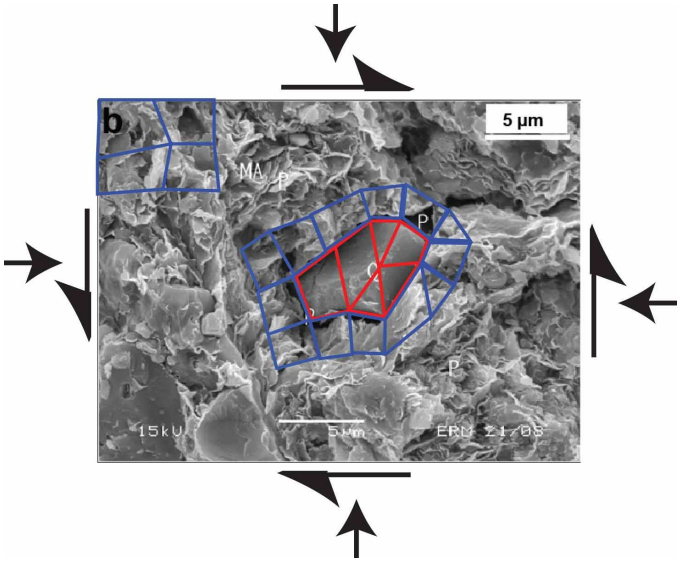

Figure 1. A Scanning Electron Microscopy (SEM) image [12] of quartz silt grain in porous clay matrix. Red finite element mesh is for the grain, and blue for the clay. The interface cracking between the two would be modeled with CSEs.

2. KINEMATICS AND GOVERNING EQUATIONS FOR STRONG DISCONTINUITIES

For strong discontinuities, the displacement field contains a spatial jump in displacement $[\![\boldsymbol{u}]\!]$ across $\mathcal{S}$ as [6]

$$\boldsymbol{u}(\boldsymbol{x},t) = \bar{\boldsymbol{u}}(\boldsymbol{x},t) + [\![\boldsymbol{u}(\boldsymbol{x},t)]\!]\; H_{\mathcal{S}}(\boldsymbol{x}) \tag{1}$$

where $\bar{\boldsymbol{u}}$ is the regular displacement field, and $H_{\mathcal{S}}$ is the Heaviside function along surface $\mathcal{S}$ (Fig.2). This displacement field leads to a singular strain $\boldsymbol{\epsilon} = \boldsymbol{\nabla}^s \boldsymbol{u}$ at $\mathcal{S}$ as

$$\boldsymbol{\epsilon} = \begin{cases} \boldsymbol{\epsilon}^1 = \boldsymbol{\epsilon}^0 + \mathrm{sym}([\![\boldsymbol{u}]\!] \otimes \boldsymbol{n})\,\delta_{\mathcal{S}} & \in \mathcal{S} \\ \boldsymbol{\epsilon}^0 & \in \Omega \backslash \mathcal{S} \end{cases} \tag{2}$$

where superscript 1 denotes a quantity along $\mathcal{S}$ and superscript 0 a quantity outside $\mathcal{S}$, where $\boldsymbol{\epsilon}^0$ is regular and $\boldsymbol{\epsilon}^1$ is singular. $\delta_{\mathcal{S}}$ is the Dirac-delta function at the discontinuity surface $\mathcal{S}$, and $\boldsymbol{n}$ is the unit normal to $\mathcal{S}$.

The local form of quasi-static, isothermal equilibrium for a body Ω with strong discontinuity is written as follows

$$\begin{aligned} \boldsymbol{\nabla}\cdot\boldsymbol{\sigma} + \boldsymbol{b} &= \boldsymbol{0} \quad \text{in } \Omega \\ \boldsymbol{\sigma}\cdot\boldsymbol{\nu} &= \boldsymbol{t}^{\sigma} \quad \text{on } \Gamma_t \\ \boldsymbol{u} &= \boldsymbol{g} \quad \text{on } \Gamma_g \\ [\![\boldsymbol{\sigma}]\!]\cdot\boldsymbol{n} &= \boldsymbol{0} \quad \text{across } \mathcal{S} \end{aligned} \tag{3}$$

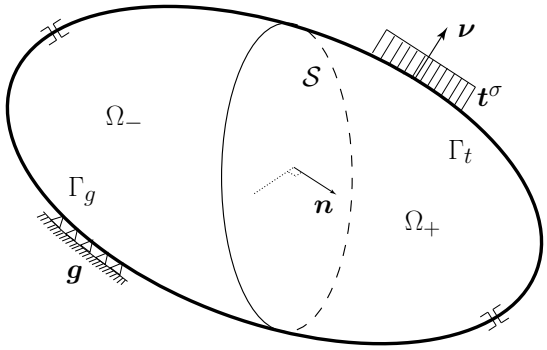

Figure 2. Body $\bar{\Omega}$ with planar strong discontinuity $\mathcal{S}$ ($\Omega = \Omega_+ \cup \Omega_-$, $\Gamma = \Gamma_t \cup \Gamma_g \cup \mathcal{S}$, $\bar{\Omega} = \Omega \cup \Gamma$).

where $\boldsymbol{\sigma}$ is the stress tensor, $\boldsymbol{b}$ the body force vector, $\boldsymbol{\nu}$ the unit normal to Γ_t, $\boldsymbol{t}^{\sigma}$ the traction on Γ_t, $\boldsymbol{g}$ the prescribed displacement on Γ_g, and $[\![\boldsymbol{\sigma}]\!]$ is the jump in stress across $\mathcal{S}$.

2.1. Weak form for embedded strong discontinuity

The weak form of 3D quasi-static equilibrium for Embedded Discontinuity finite Element (EDE) implementation is written as

$$\begin{aligned} \int_{\Omega} \boldsymbol{\nabla}^s \boldsymbol{w} : \boldsymbol{\sigma}\, dv \;=\; & \int_{\Omega} \boldsymbol{w}\cdot\boldsymbol{b}\, dv + \int_{\Gamma_t} \boldsymbol{w}\cdot\boldsymbol{t}^{\sigma}\, da \\ & + \int_{\mathcal{S}} \boldsymbol{w}\cdot([\![\boldsymbol{\sigma}]\!]\cdot\boldsymbol{n})\, da \end{aligned} \tag{4}$$

where $\boldsymbol{w} = \delta\boldsymbol{u}$ is the weighting function (or displacement variation). The traction continuity condition $[\![\boldsymbol{\sigma}]\!]\cdot\boldsymbol{n} = \boldsymbol{0}$ for a body with strong discontinuities will be used to determine bifurcation. The displacement, and its weighting function $\boldsymbol{w}$, are discretized as compatible fields (see Sect.5.1), while embedding the strong discontinuity jump in displacement $[\![\boldsymbol{u}]\!]$.

2.2. Weak form for discrete strong discontinuity represented as cohesive surface

The weak form of 2D quasi-static equilibrium for cohesize surface finite element implementation is written as

$$\begin{aligned} \int_{\Omega} \boldsymbol{\nabla}^s \boldsymbol{w} : \boldsymbol{\sigma}\, da \;=\; & \int_{\Omega} \boldsymbol{w}\cdot\boldsymbol{b}\, da + \int_{\Gamma_t} \boldsymbol{w}\cdot\boldsymbol{t}^{\sigma}\, ds \\ & - \int_{\mathcal{S}} [\![\boldsymbol{w}]\!]\cdot\boldsymbol{T}\, ds \end{aligned} \tag{5}$$

where $[\![\boldsymbol{w}]\!]$ is the jump in weighting function across discontinuity $\mathcal{S}$, implying that the jump displacement $[\![\boldsymbol{u}]\!]$ will be accounted for discretely in the Galerkin

and finite element equations, as opposed to being embedded as in the AES method. $\boldsymbol{T} = \boldsymbol{\sigma} \cdot \boldsymbol{n}$ is the traction vector on the discontinuity $\mathcal{S}$.

3. DETECTING BIFURCATION

For the EDE, detecting bifurcation depends on loss of ellipticity of the acoustic tensor for a small strain nonassociative Drucker-Prager elastoplasticity model (linear isotropic elasticity) with strong discontinuity [7] (parameters for Gosford sandstone from [9] used in the numerical example for EDE in Sect.7) and will only be briefly summarized here. For the CSE, detecting bifurcation depends on satisfying a yield criterion on a pre-defined cohesive surface.

3.1. Bifurcation for EDE with strong discontinuity

Assume the jump displacement is spatially constant along $\mathcal{S}$ and is written in terms of its magnitude ζ and direction $\boldsymbol{m}$ as

$$[\![\boldsymbol{u}(t)]\!] = \zeta(t)\, \boldsymbol{m}(t) \tag{6}$$

Note that its magnitude and direction can both vary with time, because the dilation angle ψ can evolve during post-bifurcation, and thus $\boldsymbol{m}$ can also change. For continuous traction across the discontinuity surface $\mathcal{S}$, a condition for loss of ellipticity of the acoustic tensor $\tilde{\boldsymbol{A}}$ results as

$$\begin{aligned} \det\tilde{\boldsymbol{A}} \;&=\; 0 \quad \text{for} \quad \boldsymbol{m} \neq \boldsymbol{0} \qquad (7)\\ &\tilde{\boldsymbol{A}} = \boldsymbol{n} \cdot \tilde{\boldsymbol{c}}^{ep} \cdot \boldsymbol{n} \\ &\tilde{\boldsymbol{c}}^{ep} = \boldsymbol{c}^e - \frac{\boldsymbol{c}^e : \boldsymbol{g} \otimes \boldsymbol{f} : \boldsymbol{c}^e}{\boldsymbol{f} : \boldsymbol{c}^e : \boldsymbol{g}} \\ &\boldsymbol{f} = \partial f/\partial \boldsymbol{\sigma} \;; \quad \boldsymbol{g} = \partial g/\partial \boldsymbol{\sigma} \qquad (8) \end{aligned}$$

where $\boldsymbol{c}^e$ is the elastic modulus tensor, $\tilde{\boldsymbol{c}}^{ep}$ is the continuum elastic-perfectly-plastic tangent modulus tensor, f is the yield function, and g is the plastic potential function. For strong discontinuity, the main difference in the loss of ellipticity condition is the use of the elastic-perfectly-plastic tangent modulus instead of the elastic-plastic tangent modulus [6]. The loss of ellipticity condition thus determines both the orientation of the discontinuity surface, and the stress state at which it nucleates. The deficiency with this approach is that the loss of ellipticity condition is based on the elastoplasticity model with parameters typically determined from homogeneously deforming geomaterial specimens. Cracking and fracture are associated with inhomogeneous (localized) deformation. This motivates a different approach for modeling fracture nucleation as noted in the Conclusions.

3.2. Cohesive Surface Yield Function

Following [11], we write a Mohr-Coulomb-like cohesive surface yield function with tension cap as

$$F = \sqrt{T_t^2 + (c - \chi \tan\phi)^2} - (c - T_n \tan\phi) = 0 \tag{9}$$

where T_t and T_n are the tangential and normal components of traction on the cohesive surface $\mathcal{S}$, c is cohesion, χ tensile strength, ϕ friction angle, and ψ the dilation angle.

4. POST-BIFURCATION CONSTITUTIVE MODELS

The general form of a post-bifurcation traction-displacement constitutive model is the following:

$$\begin{aligned} &\tilde{\boldsymbol{T}} = [T_n\; T_t] \\ &\quad T_n = \boldsymbol{n} \cdot \boldsymbol{\sigma} \cdot \boldsymbol{n} \;; \quad T_t = \boldsymbol{t} \cdot \boldsymbol{\sigma} \cdot \boldsymbol{n} \\ &[\![\dot{\tilde{\boldsymbol{u}}}^p]\!] = \dot{\gamma}_\delta \partial G(\tilde{\boldsymbol{T}}, \boldsymbol{q})/\partial \tilde{\boldsymbol{T}} \qquad (10)\\ &F(\tilde{\boldsymbol{T}}, \boldsymbol{q}) = 0 \qquad (11)\\ &\dot{\boldsymbol{q}} = \dot{\gamma}_\delta \boldsymbol{h}^q(\tilde{\boldsymbol{T}}, \boldsymbol{q}) \qquad (12) \end{aligned}$$

where $\tilde{\boldsymbol{T}}$ is the traction vector on $\mathcal{S}$ in the local discontinuity frame, $\boldsymbol{t}$ is the unit tangent vector on $\mathcal{S}$, $[\![\dot{\tilde{\boldsymbol{u}}}^p]\!]$ is the rate of plastic jump displacement in the local frame, $\dot{\gamma}_\delta$ is the plastic multiplier on $\mathcal{S}$, G is the plastic potential function, F is the plastic yield function, $\boldsymbol{q}$ is a vector of internal strength variables (e.g., tensile strength χ, cohesion c, friction angle ϕ, dilation angle ψ), and $\boldsymbol{h}^q$ is a vector of softening functions. Note that the post-bifurcation traction-displacement yield function is the same as the bifurcation yield function for the CSE. For the EDE, the bifurcation and post-bifurcation models are different.

Similar to both EDE and CSE, the constitutive equations are integrated using Backward Euler (implicit, first order accurate) time integration for quasi-static simulation of cracking in rock. Integrating (10)-(12) leads to

$$\begin{aligned} &\Delta\,[\![\tilde{\boldsymbol{u}}^p]\!] = \Delta\gamma_\delta (\partial G/\partial \tilde{\boldsymbol{T}})_{n+1} \qquad (13)\\ &F_{n+1} = 0 \qquad (14)\\ &\Delta \boldsymbol{q} = \Delta\gamma_\delta \boldsymbol{h}^q_{n+1} \qquad (15) \end{aligned}$$

where $\Delta(\bullet) = (\bullet)_{n+1} - (\bullet)_n$ and $n+1$ is the current time step.

At the moment, the EDE post-bifurcation constitutive model is a Mohr-Coulomb yield model with exponential softening, while the CSE model has the modification to include also a tension cap to its yield surface [11].

4.1. Evolution equations with no χ for EDE

A Mohr-Coulomb traction-displacement model with exponential softening used for the EDE is summarized as

$$\begin{aligned} F &= |T_t| - (c - T_n^* \tan\phi) \;=\; 0 \qquad (16)\\ G &= |T_t| - (c - T_n^* \tan\psi)\\ c &= c_r + (c_p - c_r)\exp\left(-\alpha_c \gamma_\delta\right)\\ &\quad \gamma_\delta = \int_0^t \dot\gamma_\delta dt \;;\;\; \dot\gamma_\delta = \cos\psi \dot\zeta\\ \phi &= \phi_r + (\phi_p - \phi_r)\exp\left(-\alpha_\phi \gamma_\delta\right)\\ \psi &= \psi_p \exp\left(-\alpha_\psi \gamma_\delta\right) \end{aligned}$$

where $T_n^* = (T_n - |T_n|)/2$ is negative for compressive normal traction and zero in tension, and the vector of internal state variables (ISVs) is

$$\boldsymbol{q} = \left[\begin{array}{cccc} c & \phi & \psi \end{array}\right]^T \qquad (17)$$

Notice $\dot\gamma_\delta$ is a shear-like plastic multiplier, as it is related to the plastic jump displacement rate magnitude $\dot\zeta$ through $\cos\psi$, which for zero dilation $\psi = 0$, $\cos\psi = 1$, and $\dot\gamma_\delta = \dot\zeta$. Subscript $(\bullet)_r$ refers to residual value, and $(\bullet)_p$ peak value. The material parameters α_c, α_ϕ, and α_ψ control the rate of softening for each internal variable. The implementation of this model using an EDE formulation is discussed briefly in Sect.5, with more details in [10].

4.2. Evolution equations with χ for CSE

The Mohr-Coulomb model in Sect.4.1 is extended to include a tension cap, and in turn parameters for Mode I (tension) and II (shear) fracture energies G_f^I and G_f^{II}, respectively, following [11]. The equations are summarized here as

$$F = \sqrt{T_t^2 + (c - \chi\tan\phi)^2} - (c - T_n\tan\phi) = 0 \qquad (18)$$

$$\begin{aligned} G &= \sqrt{T_t^2 + (c - \chi\tan\psi)^2} - (c - T_n\tan\psi)\\ \chi &= \chi_r + (\chi_p - \chi_r)\exp[-\alpha_\chi(\epsilon_n^p + \epsilon_s^p)]\\ c &= c_r + (c_p - c_r)\exp[-\alpha_c(\epsilon_n^p + \epsilon_s^p)]\\ \tan\phi &= \tan\phi_r + (\tan\phi_p - \tan\phi_r)\exp(-\alpha_\phi \epsilon_s^p)\\ \tan\psi &= (\tan\psi_p)\exp(-\alpha_\psi \epsilon_s^p)\\ &\quad \epsilon_s^p = \int_0^t \dot\epsilon_s^p dt \;;\;\; \epsilon_n^p = \int_0^t \dot\epsilon_n^p dt\\ &\quad \dot\epsilon_s^p = \frac{1}{G_f^{II}}\left\langle |T_t| + T_n^*\tan\phi\right\rangle |\dot u_t^p|\\ &\quad \dot\epsilon_n^p = \frac{1}{G_f^I}\left\langle T_n\right\rangle \dot u_n^p\\ &\left[\!\left[\dot{\tilde{\boldsymbol{u}}}^p\right]\!\right] = [\dot u_t^p, \dot u_n^p] \end{aligned}$$

where $\langle T_n\rangle = (T_n + |T_n|)/2$ is the Macauley bracket, positive in tension, otherwise zero. $\dot\epsilon_s^p$ is only activated when the tangential traction magnitude $|T_t|$ exceeds the frictional value $T_n^*\tan\phi$ in compression, while $\dot\epsilon_n^p$ is only activated when there is tension $T_n > 0$. The tensile strength χ and cohesion c can degrade both under tensile (normal) and shear (tangential) plastic jump displacement, while friction $\tan\phi$ and dilation $\tan\psi$ only degrade under shear.

5. EMBEDDED DISCONTINUITY FINITE ELEMENT (EDE)

This section summarizes an Embedded Discontinuity finite Element (EDE) implementation using an assumed enhanced strain (AES) method [5]. Further details on the hexahedral EDE implementation are found in [10]. This hexahedral EDE is used in plane strain compression simulations in the Numerical Examples section. The summary focusses on the kinematics of the enhanced EDE, the resulting Galerkin form, the yield check along $\mathcal{S}^h$, and satisfaction of continuous traction in time.

5.1 Reparameterization of displacement $\boldsymbol{u}^h$ by introduction of enhancement function $f_{\mathcal{S}}^e$ for EDE

In an EDE implementation, we want to interpolate compatible displacements at the nodes, while embedding the jump displacement within the element, such that the discrete representation of displacement field $\boldsymbol{u}^h$ is reparameterized as [6]

$$
\begin{aligned}
\boldsymbol{u}^h &= \left(\bar{\boldsymbol{u}}^h + \left[\!\left[\boldsymbol{u}^h\right]\!\right] f_{\mathcal{S}}^e\right) + \left[\!\left[\boldsymbol{u}^h\right]\!\right] \left(H_{\mathcal{S}^h} - f_{\mathcal{S}}^e\right) \\
&= \tilde{\boldsymbol{u}}^h + \hat{\boldsymbol{u}}^h \qquad (19) \\
&\quad \tilde{\boldsymbol{u}}^h = \bar{\boldsymbol{u}}^h + \left[\!\left[\boldsymbol{u}^h\right]\!\right] f_{\mathcal{S}}^e \\
&\quad \hat{\boldsymbol{u}}^h = \left[\!\left[\boldsymbol{u}^h\right]\!\right] \left(H_{\mathcal{S}^h} - f_{\mathcal{S}}^e\right) \\
&\quad M_{\mathcal{S}^h} = H_{\mathcal{S}^h} - f_{\mathcal{S}}^e
\end{aligned}
$$

where h is the spatial discretization parameter [13], $\tilde{\boldsymbol{u}}^h$ is the compatible displacement, $\hat{\boldsymbol{u}}^h$ is the enhanced displacement, $f_{\mathcal{S}}^e$ is a smooth enhancement function within element e to ensure that $\tilde{\boldsymbol{u}}^h$ is compatible and $M_{\mathcal{S}^h}$ is zero at the nodes of the EDE. We interpolate the compatible displacement using standard finite element shape functions N_a as

$$
\tilde{\boldsymbol{u}}^h(\boldsymbol{\xi}, t) = \sum_{a=1}^{n_{\text{en}}} N_a(\boldsymbol{\xi}) \boldsymbol{d}_a(t) \qquad (20)
$$

where $\boldsymbol{\xi}$ is the vector of natural coordinates and n_{en} is the number of element nodes, and $\boldsymbol{d}_a$ are the nodal displacements. To complete the EDE formulation, the enhancement function $f_{\mathcal{S}}^e$ for a hexahedral element must be determined. For a trilinear hexahedral element, various ways in which a planar strong discontinuity can cut the element are depicted in Fig.3. The procedure for determining the active nodes, and thus the enhancement function $f_{\mathcal{S}}^e$ are discussed in [10] and not repeated here.

5.2 Galerkin form of traction-displacement model

We rewrite the yield function in (16) as

$$
\begin{aligned}
F &= (\boldsymbol{\mu}^\phi \otimes \boldsymbol{n}) : \boldsymbol{\sigma} - c = 0 \qquad (21) \\
&\quad \boldsymbol{\mu}^\phi = \text{sign}(T_{\text{t}})\boldsymbol{t} + (\tan\phi)\text{sign}(T_{\text{n}}^*)\boldsymbol{n}
\end{aligned}
$$

where

$$
\text{sign}(T_{\text{n}}^*) = \begin{cases} 0 & T_{\text{n}}^* > 0 \quad \text{tension} \\ 1 & T_{\text{n}}^* < 0 \quad \text{compression} \end{cases} \qquad (22)
$$

Applying the method of weighted residuals to (21), expressing in Galerkin form [13], and dividing by $A_{\mathcal{S}^h}$, we have

$$
\frac{1}{A_{\mathcal{S}^h}} \int_{\mathcal{S}^h} \eta^h \left[(\boldsymbol{\mu}^\phi \otimes \boldsymbol{n}) : \boldsymbol{\sigma} - c\right] da = 0 \qquad (23)
$$

If we assign $\hat{\boldsymbol{H}}^h = (\boldsymbol{\mu}^\phi \otimes \boldsymbol{n})$, and we assume weighting function η^h is constant over $\mathcal{S}^h$ (which will lead to a constant jump displacement ζ over $\mathcal{S}^h$ [6]), we can write the Galerkin form as

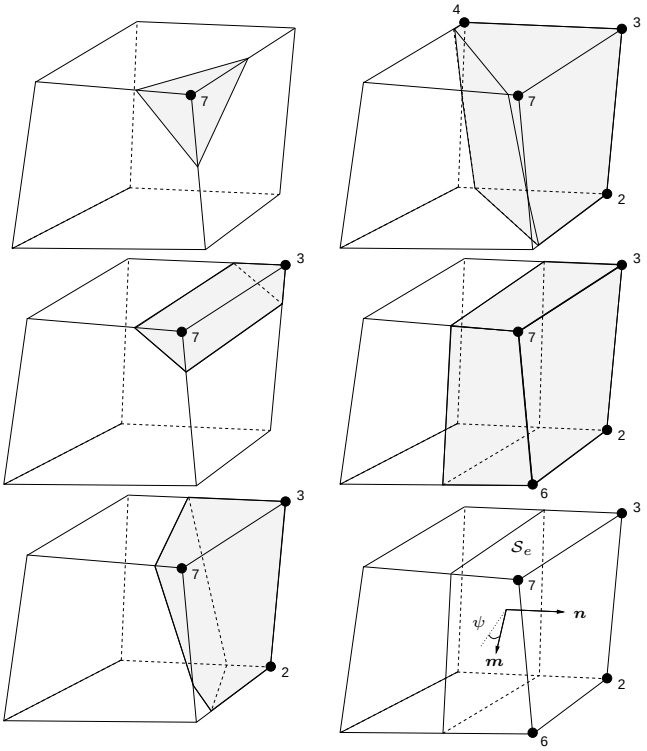

Figure 3. Embedded strong discontinuity linear hexahedral finite element.

$$
\frac{1}{A_{\mathcal{S}^h}} \int_{\mathcal{S}^h} \hat{\boldsymbol{H}}^h : \boldsymbol{\sigma} da \; - \; c \; = 0 \qquad (24)
$$

For the orthogonality condition with constant η^h

$$
\frac{1}{A_{\mathcal{S}^h}} \int_{\mathcal{S}^h} \hat{\boldsymbol{H}}^h : \boldsymbol{\sigma}^h da = \frac{1}{V_{\text{loc}}^h} \int_{\Omega_{\text{loc}}^h} \hat{\boldsymbol{H}}^h : \boldsymbol{\sigma}^h dv \qquad (25)
$$

which means we can write the Galerkin form as an integration over the volume of the element, allowing us to use the stresses evaluated at the Gauss points to calculate the traction $\boldsymbol{T}$ along $\mathcal{S}^h$.

In summary, the complete Galerkin form written in residual form is

$$
\begin{aligned}
R(\boldsymbol{\sigma}) &= \int_{\Omega^h} \boldsymbol{\nabla}\tilde{\boldsymbol{w}}^h : \boldsymbol{\sigma}^h dv - \int_{\Omega^h} \tilde{\boldsymbol{w}}^h \cdot \boldsymbol{b} dv \\
&\quad - \int_{\Gamma_t^h} \tilde{\boldsymbol{w}}^h \cdot \boldsymbol{t}^\sigma da = 0 \qquad (26) \\
r(\boldsymbol{\sigma}, \boldsymbol{q}) &= \frac{1}{V_{\text{loc}}^h} \int_{\Omega_{\text{loc}}^h} \hat{\boldsymbol{H}}^h : \boldsymbol{\sigma} dv - c = 0 \qquad (27)
\end{aligned}
$$

We will take advantage of the fact that ζ is discontinuous between elements, a result of the assumed enhanced strain implementation, and condense out (27)

when solving for the compatible displacements at the nodes. Linearization for solution by the Newton-Raphson method is summarized in [10].

5.3 Yield check along $\mathcal{S}^h$

We calculate the trial yield value along $\mathcal{S}^h$ by

$$F^{\rm tr} \;=\; \frac{1}{V^h_{\rm loc}}\int_{\Omega^h_{\rm loc}} (\hat{\boldsymbol{H}}^h)^{\rm tr} : \boldsymbol{\sigma}^{\rm tr} dv \;-\; c_n$$

where

$$(\hat{\boldsymbol{H}}^h)^{\rm tr} = (\boldsymbol{\mu}^{\phi_n} \otimes \boldsymbol{n})$$
$$\boldsymbol{\mu}^{\phi_n} = \text{sign}(T^{\rm tr}_{\rm t})\boldsymbol{t} + (\tan\phi_n)\text{sign}[(T^*_{\rm n})^{\rm tr}]\boldsymbol{n}$$

If $F^{\rm tr} > 0$ there is yielding along $\mathcal{S}^h$, and ζ will evolve. Otherwise, the internal variables and ζ will be held fixed.

5.4 Continuous stress in time at bifurcation point

In order to ensure that the stress is continuous in time at the point of bifurcation, the peak cohesion c_p is calculated from (27) within an element e as

$$c_p = \frac{1}{V^e_{\rm loc}}\int_{\Omega^e_{\rm loc}} \hat{\boldsymbol{H}}^e : \boldsymbol{\sigma}_n dv \tag{28}$$

where $V^e_{\rm loc}$ is the localized element volume, $\Omega^e_{\rm loc}$ its domain, $\hat{\boldsymbol{H}}^e$ its enhancement function multiplier, and $\boldsymbol{\sigma}_n$ the converged stress from the past time step t_n before bifurcation was detected in the element e.

6. ELASTO-PLASTIC (EP) AND RIGID-PLASTIC (RP) COHESIVE SURFACE ELEMENTS (CSE)

The elasto-plastic (EP) CSE finite element implementation follows directly from the weak form in (5), while the rigid-plastic (RP) CSE implementation requires modification to include a Lagrange multiplier to enforce a constraint (no additional sliding/opening) cohesive surface when plasticity is not active.

6.1 EP CSE implementation

Taking the Galerkin approximation of the weak form in (5), and introducing finite element interpolation functions for the bulk continuum elements and CSEs, we have the nonlinear matrix finite element equations for EP CSE

$$\begin{aligned}
\boldsymbol{F}^{INT}(\boldsymbol{d}) \;&=\; \boldsymbol{F}_f + \boldsymbol{F}_t - \boldsymbol{F}_{cse}(\boldsymbol{d}) \qquad (29)\\
\boldsymbol{F}^{INT}(\boldsymbol{d}) &= \mathop{\mathbf{A}}_{e=1}^{n_{el}} \int_{\Omega^e} (\boldsymbol{B}^e)^T \cdot \boldsymbol{\sigma}^h(\boldsymbol{d}^e) da\\
\boldsymbol{F}_f &= \mathop{\mathbf{A}}_{e=1}^{n_{el}} \int_{\Omega^e} (\boldsymbol{N}^e)^T \cdot \boldsymbol{b} da\\
\boldsymbol{F}_t &= \mathop{\mathbf{A}}_{e=1}^{n_{el}} \int_{\Gamma^e_t} (\boldsymbol{N}^e)^T \cdot \boldsymbol{t}^\sigma ds\\
\boldsymbol{F}_{cse} &= \mathop{\mathbf{A}}_{e=1}^{n_{el,cse}} \int_{\mathcal{S}^e} (\boldsymbol{N}^{cse})^T \cdot \boldsymbol{T}^h ds
\end{aligned}$$

where $\mathop{\mathbf{A}}_{e=1}^{n_{el}}$ is the element assembly operator over number of elements n_{el}, $\boldsymbol{N}^e$ is the bulk element shape function matrix, $\boldsymbol{B}^e$ the bulk strain-displacement matrix, and $\boldsymbol{N}^{cse}$ the CSE shape function matrix. The CSE traction vector in the global coordinate Cartesian frame $\boldsymbol{T}^h$ is related to the local frame $\tilde{\boldsymbol{T}}^h$ through the orthogonal rotation matrix $\boldsymbol{\Lambda}$, such that $\boldsymbol{T}^h = \boldsymbol{\Lambda}^T \cdot \tilde{\boldsymbol{T}}^h$. The EP CSE local traction vector $\tilde{\boldsymbol{T}}$ is related to the jump elastic displacement in the local frame through an elastic modulus matrix $\boldsymbol{K}^e$ as, written in rate form,

$$\dot{\tilde{\boldsymbol{T}}} = \boldsymbol{K}^e \cdot [\![\dot{\tilde{\boldsymbol{u}}}^e]\!] = \boldsymbol{K}^e \cdot \left([\![\dot{\tilde{\boldsymbol{u}}}]\!] - [\![\dot{\tilde{\boldsymbol{u}}}^p]\!]\right) \tag{30}$$

$$\boldsymbol{K}^e = \begin{bmatrix} k_t & 0 \\ 0 & k_n \end{bmatrix}$$

where k_t is the elastic tangential stiffness, and k_n the elastic normal stiffness. This stress rate equation is integrated using Backward Euler, similar to the plasticity equations in (13)-(15). When the stress-rate equation is combined with these equations, the resulting nonlinear equations are solved at t_{n+1} for $\tilde{\boldsymbol{T}}$, $\boldsymbol{q}$, and $\Delta\gamma_\delta$ using a local Newton-Raphson algorithm on the following residual

$$\boldsymbol{R} = \begin{bmatrix} \tilde{\boldsymbol{T}}_{n+1} - \tilde{\boldsymbol{T}}^{tr}_{n+1} + \Delta\gamma_\delta \boldsymbol{K}^e \cdot \partial G/\partial \tilde{\boldsymbol{T}}_{n+1} \\ \Delta\boldsymbol{q} - \Delta\gamma_\delta \boldsymbol{h}^q_{n+1} \\ F_{n+1} \end{bmatrix} = \boldsymbol{0} \tag{31}$$

where $\tilde{\boldsymbol{T}}^{tr}_{n+1} = \tilde{\boldsymbol{T}}_n + \boldsymbol{K}^e \cdot \Delta[\![\tilde{\boldsymbol{u}}]\!]$ is the trial CSE traction in the local frame. Likewise, a local consistent tangent $\partial\tilde{\boldsymbol{T}}/\partial[\![\tilde{\boldsymbol{u}}]\!]$ can be derived (refer to [14] for more details), which fits into the global consistent tangent used to solve (29) using Newton-Raphson. Section 7 will present numerical examples that demonstrate the application of these algorithms.

6.2 RP CSE implementation

For RP CSE, elastic jump displacement is zero $[\![\tilde{\boldsymbol{u}}^e]\!] = \mathbf{0}$, such that the total jump displacement equals the plastic jump displacement $[\![\tilde{\boldsymbol{u}}]\!] = [\![\tilde{\boldsymbol{u}}^p]\!]$. When the trial yield function $F^{tr} < 0$, a constraint must be satisfied to hold the cohesive surface rigid until $F^{tr} > 0$. F^{tr} is calculated from the cohesive traction vector used to constrain the cohesize surfaces. These traction vectors will be the Lagrange multipliers enforcing the constraint. The weak form (5) is modified to account for the constraint in the Cartesian coordinates

$$\boldsymbol{h} = [\![\boldsymbol{u}]\!]_{n+1} - [\![\boldsymbol{u}]\!]_n = \mathbf{0} \tag{32}$$

as

$$\begin{aligned} &\int_\Omega \boldsymbol{\nabla}^s \boldsymbol{w} : \boldsymbol{\sigma} da + \int_{\mathcal{S}_c} \boldsymbol{\eta} \cdot (\boldsymbol{\lambda} + r\boldsymbol{h}) ds \\ &= \int_\Omega \boldsymbol{w} \cdot \boldsymbol{b} da + \int_{\Gamma_t} \boldsymbol{w} \cdot \boldsymbol{t}^\sigma ds - \int_{\mathcal{S}} [\![\boldsymbol{w}]\!] \cdot \boldsymbol{T} ds \\ &\int_{\mathcal{S}_c} \boldsymbol{\beta} \cdot \boldsymbol{h} ds = 0 \end{aligned} \tag{33}$$

where $\boldsymbol{\eta} = \delta\boldsymbol{h}$ and $\boldsymbol{\beta} = \delta\boldsymbol{\lambda}$ are the weighting functions, with $\boldsymbol{\lambda}$ the Lagrange multiplier (cohesive surface tractions when constraint $\boldsymbol{h} = \mathbf{0}$ is satisfied). Equations (33) lead to a coupled system of finite element equations to solve using Newton-Raphson (details in [14, 15]). Aside from the Lagrange multiplier to enforce the constraint, the main difference between RP and EP CSE implementations is that the local equations to solve at t_{n+1} for $\tilde{\boldsymbol{T}}$, $\boldsymbol{q}$, and $\Delta\gamma_\delta$ using a local Newton-Raphson algorithm are the plasticity equations expressed in residual form as

$$\boldsymbol{R} = \begin{bmatrix} \Delta [\![\tilde{\boldsymbol{u}}]\!] - \Delta\gamma_\delta \partial G / \partial \tilde{\boldsymbol{T}}_{n+1} \\ \Delta\boldsymbol{q} - \Delta\gamma_\delta \boldsymbol{h}^q_{n+1} \\ F_{n+1} \end{bmatrix} = \mathbf{0} \tag{34}$$

The challenge with this implementation is encountered during the first plastic time step (when $F^{tr} > 0$ is first detected at an integration point; we use nodal integration for $\mathcal{S}^h$ and $\mathcal{S}^h_c$) and first global iteration, when $\Delta\gamma_\delta = 0$, which leads to non-unique solution of $\tilde{\boldsymbol{T}}$, $\boldsymbol{q}$, and $\Delta\gamma_\delta$. To circumvent this difficulty, we use $F_{n+1} = 0$ to provide an initial value for $\Delta\gamma_\delta$ in the first plastic step and first global iteration, which is then iterated to reach its final converged value at time t_{n+1}. We use the elastic predictor, plastic corrector form for the traction vector $\tilde{\boldsymbol{T}}_{n+1} = \tilde{\boldsymbol{T}}^{tr}_{n+1} - \Delta\gamma_\delta \boldsymbol{K}^e \cdot \partial G / \partial \tilde{\boldsymbol{T}}_{n+1}$ in $F_{n+1} = 0$ to provide the initial value $\Delta\gamma_\delta$, and only in the first global iteration of the first plastic time step. The elastic stiffness matrix $\boldsymbol{K}^e$ is not used beyond the first plastic step and first global iteration. Subsequent iterations use equations (34) to solve for the variables, as is demonstrated in the numerical examples.

7. NUMERICAL EXAMPLES

2D plane strain compression examples demonstrate the aforementioned models and EDE and CSE implementations. The EDE element is hexahedral, but run in plane strain condition to compare to the CSE 2D plane strain implementations.

The linear isotropic elasticity parameters for each model are Young's modulus $E = 1.5e7$Pa and Poisson's ratio $\nu = 0.3$. The plasticity parameters used for the EDE, and EP and RP CSE models are listed in Table 1. You will notice that two values are used for the elastic stiffnesses k_t and k_n for the EP CSE example, and in turn two values for the softening coefficients α_χ and α_c. The different values for the elastic stiffnesses were chosen to show the difference in force-displacement response in Fig.5, while it was found that in order to converge, lesser softening coefficients were also needed when the elastic stiffness of the EP CSE was reduced.

The meshes used for EDE and CSE examples are shown in Fig.4, with boundary conditions showing prescribed axial displacement, and lateral confining pressure of 20kPa. One trilinear hexahedral element (with out-of-plane faces constrained in normal displacement) is used for the EDE example, while two bulk elastic bilinear quadrilateral elements and one linear CSE element are used for the CSE examples.

For the parameters in Table 1, the resulting axial force versus prescribed axial displacement is plotted for each example in Fig.5. For the EDE example, there is an increase in stress after plastic yielding (commonly observed for plane strain loading with softening), and then bifurcation detected ($\det\tilde{\boldsymbol{A}} = 0$) at ≈ 3700N/m, followed by a pronounced exponential softening and residual stress value. The deformed mesh at end of loading is shown in Fig.6(left). Note that the discrete crack is not observed in the EDE deformed mesh, but its effect of shearing down and to the left is observed, along with the softening response. This is why we call such methods "embed-

symbol	EDE	EP CSE	RP CSE
k_t	·	1e9, 1e8 Pa/m	·
k_n	·	1e9, 1e8 Pa/m	·
G_f^I	·	1e4 J/m^2	1e4 J/m^2
G_f^{II}	·	1e4 J/m^2	1e4 J/m^2
χ_p	·	15680 Pa	15680 Pa
χ_r	·	0	0
c_p	calculated	9053 Pa	9053 Pa
c_r	0	0	0
ϕ_p	0.5236 rad	0.5236 rad	0.5236 rad
ϕ_r	0	0	0
ψ_p	0.087 rad	0.087 rad	0.087 rad
α_χ	·	2e3, 2e2	2e3
α_c	5e2 1/m	2e3, 2e2	2e3
α_ϕ	5e2 1/m	9e2	9e2
α_ψ	5e2 1/m	9e2	9e2

Table 1. Parameters for plane strain compression: post-bifurcation, exponential softening plasticity models. Note that the peak cohesion c_p for the EDE is calculated from (28) in order to ensure that the stress is continuous in time at bifurcation. This same value is used for c_p and $\chi_p = c_p \cot \phi_p$ in the CSE models.

ded discontinuity" because you do not explicitly see the crack splitting a bulk continuum element, but its effect is felt by the element. On the other hand, for the CSE examples, the CSE orientation and position is *a-priori* defined as shown in Fig.4. For this example, its location and orientation were chosen to match that predicted by det$\tilde{\boldsymbol{A}} = 0$ for the EDE element (its location is through the center of the element, and for this loading there is no preference for the two discontinuity normal angles solved by det$\tilde{\boldsymbol{A}} = 0$, so one was chosen arbitrarily). The deformed mesh for EP CSE (similar for RP CSE) is shown in Fig.6(right).

There are three axial force versus prescribed axial displacement curves shown in Fig.5 for the CSE. The open circle curve denotes the RP CSE result, which follows the EDE elastic loading curve exactly until plastic CSE is activated by $F^{tr} > 0$. The EP CSE case $k_n = k_t = 1e9$Pa/m is nearly the same as the RP CSE case, with slight difference in the elastic loading curve. For another (apparently) large value of elastic stiffness along the CSE, for EP CSE case $k_n = k_t = 1e8$Pa/m, the elastic loading curve is noticeably different than the more stiff EP CSE case, the RP CSE case, and the EDE case. This supports our

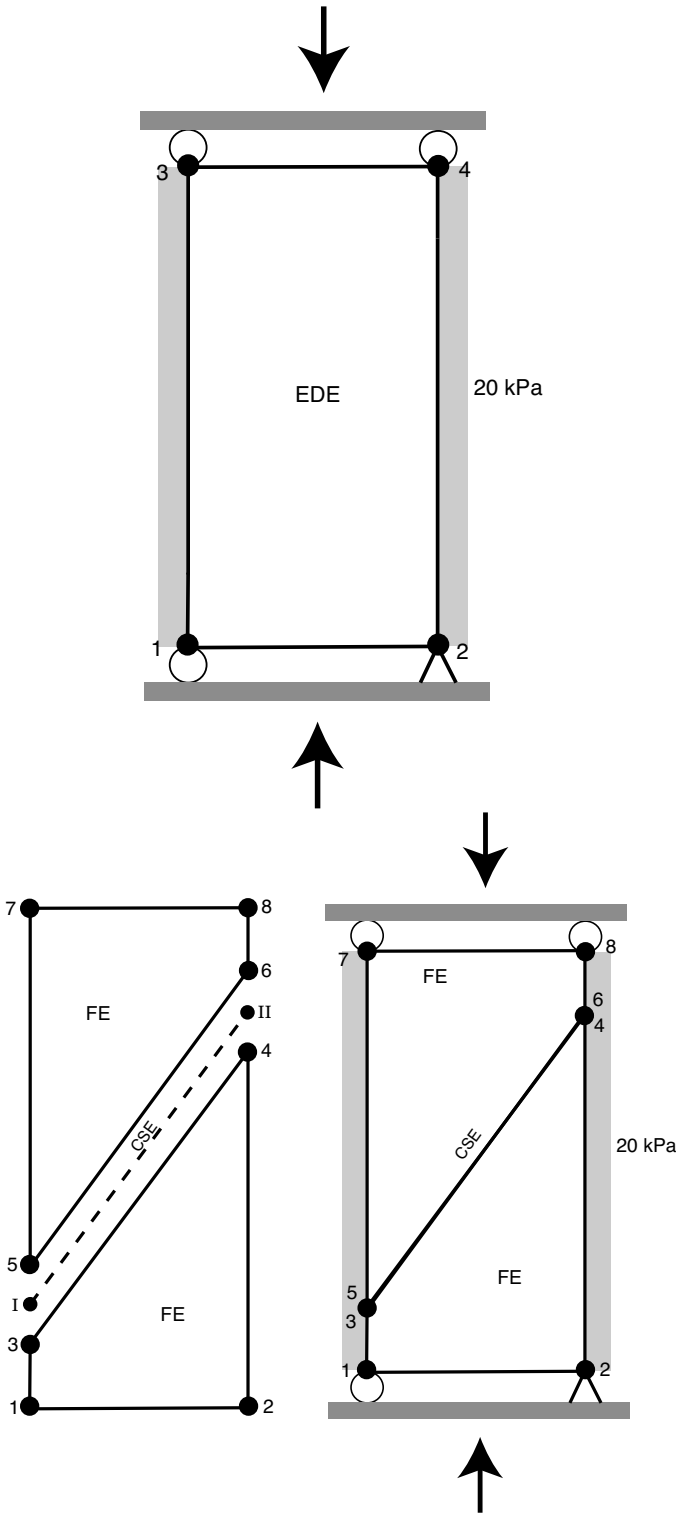

Figure 4. (top) mesh with one EDE, and (bottom) mesh with two elastic FEs and one elasto-plastic or rigid-plastic CSE.

conclusion that although implementing an EP CSE is easier than a RP CSE, care must be taken in choosing k_n and k_t if these are penalty parameters (no actual elastic stiffness associated with the CSE since it is zero thickness). It is preferable to use a RP CSE or EDE, where such penalty parameters are not needed. The resulting internal state variable (ISV) evolution

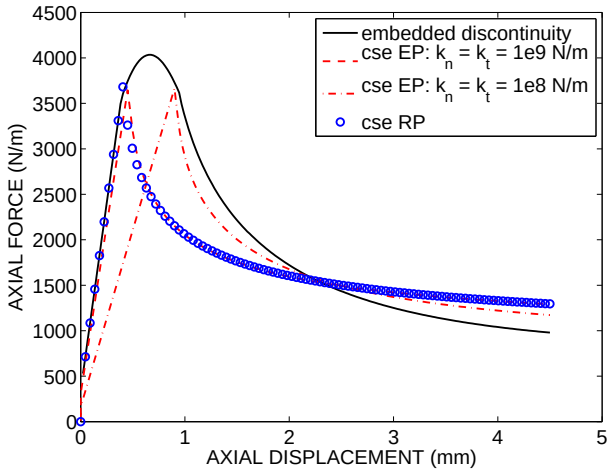

Figure 5. Axial force versus axial displacement for EDE, EP CSE (two sets of elastic parameters), and RP CSE.

post-bifurcation is shown in Figs.7-9. The evolution of the tensile strength variable χ is not shown because it is not used in the EDE model, and thus for the moment full comparison cannot be made between the models. The evolution of ISVs is the same for EP and RP CSE implementations, assuming the same parameters are chosen.

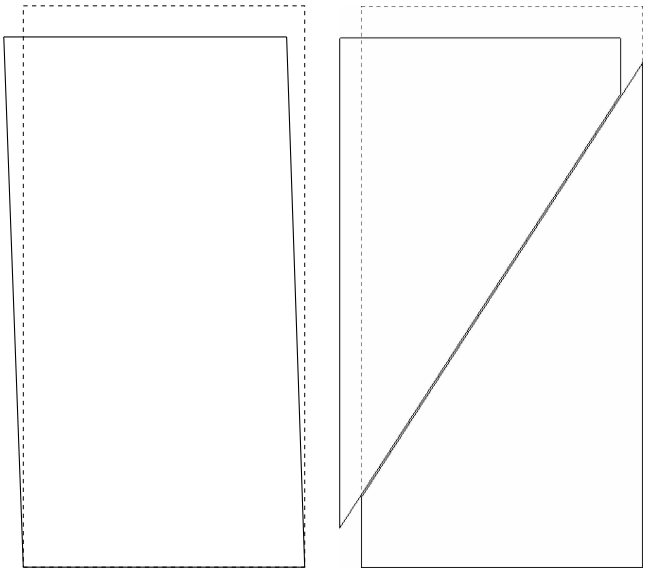

Figure 6. Deformed meshes (solid lines) for EDE (left) and EP CSE (right). Dashed lines show undeformed meshes.

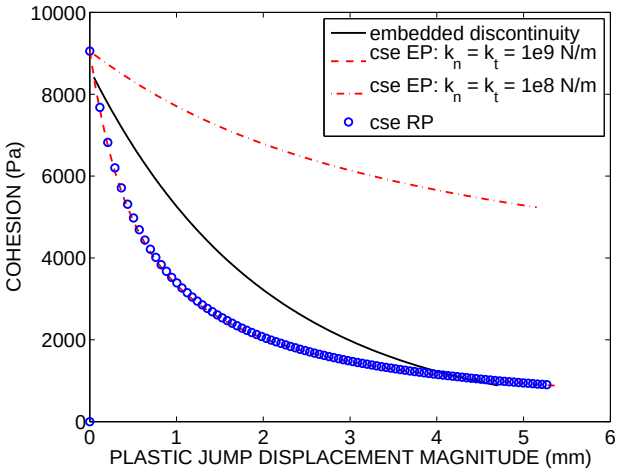

Figure 7. Cohesion c versus magnitude of plastic jump displacement $\| [\![\boldsymbol{u}^p]\!] \|$ for EDE, EP CSE (two sets of elastic parameters), and RP CSE.

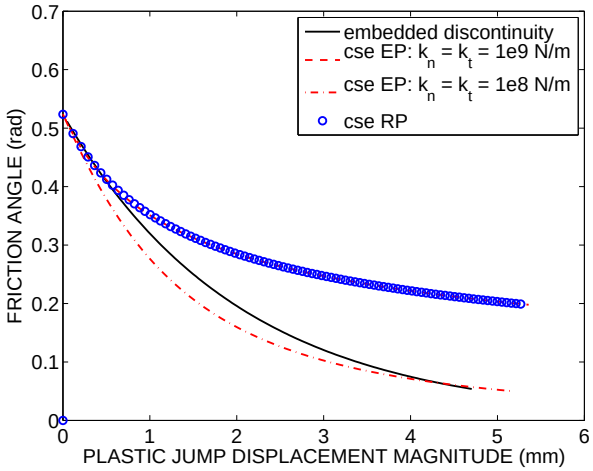

Figure 8. Friction angle ϕ versus magnitude of plastic jump displacement $\| [\![\boldsymbol{u}^p]\!] \|$ for EDE, EP CSE (two sets of elastic parameters), and RP CSE.

8. CONCLUSIONS

The paper set out to provide an initial comparison of two different ways to model cracking/fracture in rocks: (1) Embedded Discontinuity Element (EDE), and (2) Elasto-Plastic (EP) and Rigid-Plastic (RP) Cohesive Surface Element (CSE). The EDE is inherently RP. To compare the implementations related to the numerical examples presented, we provide this list:

1. orientation of crack cohesive surface in EDE determined by loss of ellipticity ($\det \tilde{\boldsymbol{A}} = 0$), and its location is chosen at the center of the element, while in CSE the surface orientation

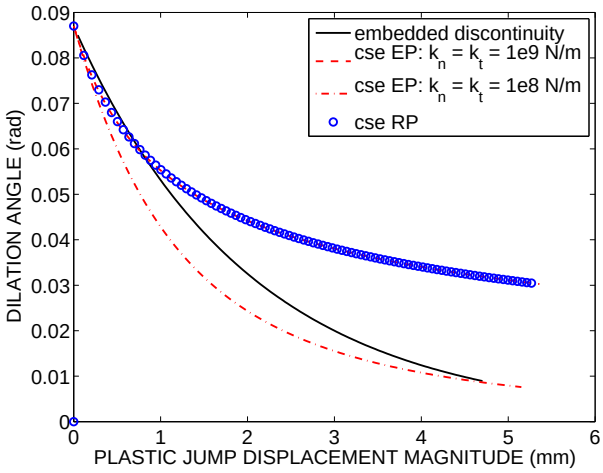

Figure 9. Dilation angle ψ versus magnitude of plastic jump displacement $\| [\![\boldsymbol{u}^p]\!] \|$ for EDE, EP CSE (two sets of elastic parameters), and RP CSE.

and location is predefined

2. activation of discontinuity surface plasticity is governed by yield criterion $F = 0$ for both EDE and CSE (EP and RP) models

3. EDE and RP models do not assume artificial elastic compliance on discontinuity surface, whereas CSE EP model does, and the elastic parameters k_n and k_t are treated as penalty parameters, which must be chosen with care

4. the CSE RP model uses Lagrange multipliers to constrain the cohesive surface before activation to plastic loading $F = 0$, while CSE EP uses penalty parameters (interfacial stiffnesses k_n and k_t) to 'constrain' the surface before plasticity

Each approach has its advantages and disadvantages:

- in AES, crack tip stress fields are not resolved, whereas with mesh refinement the CSE approach can resolve the crack tip field accurately (note: X-FEM has the advantage of embedded crack-tip stress field analytical solutions, but for future multiscale modeling, where grain-scale models resolve the crack tip solution, an X-FEM or AES method should yield similar results, with AES being potentially more computationally efficient)
- the CSE approach can resolve cohesive surfaces between dissimilar materials, such as a silt grain embedded in a clay matrix in a shale (Fig.1), whereas AES (as currently formulated) cannot

In the future, we plan to use the two approaches simultaneously in a multiscale modeling method to predict fracture in rock, using RP CSE to resolve interfacial cohesive surface strengths between grains and matrix materials, and the EDE as the macroscale model of fracture to which to upscale the grain-scale prediction by RP CSE. It is desired to simulate these problems as quasi-static, thus the formulations and implementations in this paper were presented for quasi-static loading, requiring consistent tangents, etc, provided for nonlinear Newton-Rapshon solution. Forthcoming papers will expound on the details of the finite element implementations, and numerical examples with application to realistic fracture problems in rocks.

9. ACKNOWLEDGEMENTS

The stimulus for this work was originated through an informal collaboration with Professor Majid Manzari at George Washington University.

REFERENCES

[1] Sanz, P.F., Pollard, D.D., Allwardt, P.F., and R.I. Borja. 2008. Mechanical models of fracture reactivation and slip on bedding surfaces during folding of the asymmetric anticline at Sheep Mountain, Wyoming. *Journal of Structural Geology* 30(9):1177-1191.

[2] Caballero, A., Carol, I. and C.M. Lopez. 2006. A meso-level approach to the 3D numerical analysis of cracking and fracture of concrete materials. *Fatigue Fract. Eng. Mater. Struct.* 29(12):979-991.

[3] Dolbow, J., Moes, N., and T. Belytschko. 2001. An extended finite element method for modeling crack growth with frictional contact. *Comp. Meth. App. Mech. Engr.* 190:6825-46.

[4] Borja, R.I. 2008. Assumed enhanced strain and the extended finite element methods: A unification of concepts. *Comp. Meth. App. Mech. Engr.* 197(33-40):2789-2803.

[5] Simo, J.C., and M.S. Rifai. 1990. A class of mixed assumed strain methods and the method of incompatible modes. *Int. J. Numer. Methods Eng.* 29:1595–1638.

[6] Simo, J.C., J. Oliver, and F. Armero. 1993. An analysis of strong discontinuities induced by strain-softening in rate-independent inelastic solids. *Comput. Mech.* 12: 277–296.

[7] Regueiro, R.A., and R.I. Borja. 1999. Finite element model of localized deformation in frictional materials taking a strong discontinuity approach. *Finite Elem. Anal. Des.* 33:283–315.

[8] Borja, R.I., and R.A. Regueiro. 2001. Strain localization in frictional materials exhibiting displacement jumps. *Comput. Methods Appl. Mech. Engrg.* 190:2555–80.

[9] Regueiro, R.A., and R. I. Borja. 2001. Plane strain finite element analysis of pressure sensitive plasticity with strong discontinuity. *Int. J. Solids Struct.* 38:3647–72.

[10] Regueiro, R.A. 2006. Embedded discontinuity finite element modeling of three-dimensional strong discontinuities in rocks, ARMA/USRMS 06-1069.

[11] Carol, I., Prat, P.C., and C.M. Lopez. 1997. A normal/shear cracking model. Application to discrete crack analysis. *J. Eng. Mech.* 123:765-773.

[12] Wenk, H.-R., Voltolini, M., Mazurek, M., Van Loon, L.R., and A. Vinsot. 2008. Preferred orientations and anisotropy in shales: Callovo-oxfordian shale (France) and opalinus clay (Switzerland). *Clays and Clay Minerals* 56(3):285-306.

[13] T.J.R. Hughes. 1987. *The Finite Element Method*. Prentice-Hall: New Jersey.

[14] S.-K. Yu. 2010. *Two-dimensional cohesive surface elements for quasi-static elasto-plastic/rigid-plastic pressure-sensitive cohesive surface models*. PhD dissertation, in preparation. University of Colorado at Boulder.

[15] P.A. Klein, S.X. McFadden, D.J. Bammann, Y. Hammi, J.W. Foulk, and B.R. Antoun. 2003. *A mechnism-based approach to modeling ductile fracture*, SAND2003-8804, Sandia National Laboratories Report.

[16] E. Lorentz. 2008. A mixed interface finite element for cohesive zone models. *Comput. Methods Appl. Mech. Engrg.* 198:302-317.